ELSEVIER

Journal of Nuclear Materials 295 (2001) 193–204

journal of nuclear materials

www.elsevier.nl/locate/jnucmat

The effects of moisture on LiD single crystals studied by temperature-programmed decomposition

L.N. Dinh [a,*], C.M. Cecala [b], J.H. Leckey [b], M. Balooch [a]

[a] *Chemistry and Materials Science, Lawrence Livermore National Laboratory, P.O. Box 808, L-350, Livermore, CA 94551, USA*
[b] *Lockheed Martin Energy Systems, Oak Ridge, TN, USA*

Received 7 November 2000; accepted 6 March 2001

Abstract

Temperature-programmed decomposition (TPD) technique was performed on LiOH powders and LiD single crystals previously exposed to different moisture levels. Our results show that the LiOH decomposition process is rate-limited by an inward moving reaction front mechanism with an activation energy barrier of ~122–149 kJ/mol. The LiOH structure is stable even if kept at 320 K. However, LiOH structures formed on the surface of LiD single crystals during moisture exposure at low dosages may have multiple activation energy barriers, some of which may be much lower than 122 kJ/mol. The rate-limiting mechanism for the decomposition of LiOH structures with reduced activation energy barriers is consistent with a unimolecular nucleation model. We attribute the lowering of the activation energy barrier for the LiOH decomposition to the existence of sub-stoichiometric $Li(OH)_x$ with $x < 1$ and cracks, broken bonds, and other disorders in the LiOH structures formed at low levels of moisture exposure. These defective LiOH structures may decompose significantly over many years of storage even at room temperature. At high moisture exposure levels, $LiOH \cdot H_2O$ formation is observed. The release of H_2O molecules from $LiOH \cdot H_2O$ structure has small activation energy barriers in the range of 48–69 kJ/mol and follows a unimolecular nucleation process. The loosely bonded H_2O molecules in the $LiOH \cdot H_2O$ structure can be easily pumped away at room temperature in a reasonable amount of time. Our experiments also suggest that handling LiD single crystals at an elevated temperature of 340 K or more reduces the growth rate of LiOH and $LiOH \cdot H_2O$ significantly.

PACS: 28.52.Fa

1. Introduction

As a result of exposure to water vapor during routine handling, a corrosion layer will form on the surface of lithium deuteride. It is believed that depending on the conditions of exposure, LiOH and/or Li_2O are formed with some $LiOH \cdot H_2O$ formation at higher exposure levels. In a closed system, LiOH will react with LiD to generate hydrogen gas (H_2, HD, D_2). A recent literature review indicates that there are still many unanswered questions concerning the interaction of LiD with H_2O [1,2]. A few models have been proposed to explain some of the observed results of H_2O exposure [1,2]. However, more studies are needed to obtain insight on the mechanism involved for such a complex reaction system and to handle LiD in different environments. Additionally, it is desirable to determine the kinetic parameters for the reactions resulting from H_2O exposure in order to model the long-term behavior of LiD, previously exposed to moisture, in a closed system.

In this report, temperature-programmed decomposition (TPD) experiments have been conducted on LiOH powders and LiD single crystals under a variety of moisture exposure conditions. The activation energies for the LiOH decomposition have been deter-

* Corresponding author. Tel.: +1-925 422 4271; fax: +1-925 422 6892.
E-mail address: dinh1@llnl.gov (L.N. Dinh).

PII: S0022-3115(01)00548-7

mined over a range of H_2O exposure levels. The decomposition of LiOH during storage is discussed and method for reducing long-term outgassing is also presented.

2. Experimental methods

LiOH powders were prepared by reacting LiD powders in a beaker containing liquid H_2O over an extended period of time (many days). Water was allowed to evaporate at room temperature, leaving the powders behind. The powders were then wrapped inside a Pt envelope. The side of the envelope facing the mass-spectrometer was perforated with many holes over the entire surface. The loaded foil was held fixed to a sample holder by way of three mechanical clamps and transferred into an ultrahigh vacuum (UHV) chamber with a base pressure of 10^{-6} Pa (4×10^{-7} Pa in the detector chamber) through a differentially pumped load lock. The sample was pumped in the UHV chamber for a few hours to remove H_2O molecules that were loosely bonded to the powders. A type K thermocouple was inserted between the Pt envelope surface and a clamp holding the envelope for temperature measurement. The samples were heated by passing currents through a tungsten coil located 2 mm behind the samples. The detector chamber is equipped with a quadrupole mass spectrometer (QMS) and has been described in detail elsewhere [3].

Some LiD single crystals were cleaved in air along the {1 0 0} planes, then exposed to ambient air for a certain length of time prior to TPD experiment. Others were cleaved in a glove bag, which was attached directly to the entrance port of the TPD load chamber and backfilled with N_2 (10–20% relative humidity). In a TPD experiment, the cleaved LiD sample was held fixed to a sample holder by way of three mechanical clamps and transferred into the main TPD chamber as mentioned above. The samples, which had been cleaved in the glove bag, were also heat-treated at a predetermined temperature for a given length of time, cooled down to room temperature, then exposed to a studied level of moisture for a planned amount of time. All samples were pumped for some time (a few hours to a few days) prior to TPD experiments.

The dimensions and morphologies of LiOH powders and LiOH films were examined by a scanning electron microscope (SEM) in secondary electron detection mode. All samples were transported in air with 30–40% relative humidity prior to SEM works. LiOH powders and thick LiOH films on LiD substrate also required one or two monolayers of surface Au overcoating prior to loading into the SEM chamber to mitigate charging problem.

3. Analysis techniques

During TPD, LiOH decomposes by the overall reaction

$$2\mathrm{LiOH\ (s)} \rightarrow \mathrm{Li_2O\ (s)} + \mathrm{H_2O\ (g)}. \tag{1}$$

The work by McIntyre [4] on measuring the isothermal weight loss of LiOH powders, reported by Meyers [1] suggested that the LiOH to Li_2O conversion for LiOH spherical grains is rate-limited by a reaction front moving at a constant rate into a grain of radius R. The rate equation for a solid-state reaction following this model has been well documented [5–8], and is represented here in detail.

For a reaction front moving at a constant rate, κ (nm/s), into a spherical grain of radius R

$$\frac{\mathrm{d}r}{\mathrm{d}t} = -\kappa \tag{2}$$

or

$$r = -\kappa t + R, \tag{3}$$

and the reacted fraction α is

$$\alpha = 1 - \frac{r^3}{R^3} = 1 - \left(1 - \frac{\kappa}{R}t\right)^3 \tag{4}$$

or

$$(1-\alpha)^{2/3} = \left(1 - \frac{\kappa}{R}t\right)^2 = \left(\frac{r}{R}\right)^2. \tag{5}$$

From Eqs. (4) and (5)

$$\frac{\mathrm{d}\alpha}{\mathrm{d}t} = 3\left(\frac{r}{R}\right)^2 \frac{\kappa}{R} = 3\left(\frac{4\pi r^2}{4\pi R^2}\right)\frac{\kappa}{R}. \tag{6}$$

From Eq. (6), it is seen that the fractional reaction rate is inversely proportional to the radius of the grain, R, and the interface surface of the reaction front, which changes with time. Substituting (5) into (6), we obtain

$$\frac{\mathrm{d}\alpha}{\mathrm{d}t} = 3\frac{\kappa}{R}(1-\alpha)^{2/3} = 3\frac{\kappa_0\,\mathrm{e}^{-(E/RT)}}{R}(1-\alpha)^{2/3}. \tag{7}$$

Eq. (7) is of the general form

$$\frac{\mathrm{d}\alpha}{\mathrm{d}t} = kf(\alpha) = \upsilon\,\mathrm{e}^{-(E/RT)}f(\alpha) \tag{8}$$

with $f(\alpha) = (1-\alpha)^{2/3}$ and $k = \upsilon\,\mathrm{e}^{-(E/RT)} = 3(\kappa_0/R)\,\mathrm{e}^{-(E/RT)}$.

If a linear heating schedule of $T = T_0 + \beta t$ is employed:

$$\frac{\mathrm{d}\alpha}{\mathrm{d}T} = \left(\frac{\upsilon}{\beta}\,\mathrm{e}^{-(E/RT)}\right)f(\alpha). \tag{9}$$

In the integral form

$$g(\alpha) \equiv \int_0^{\alpha} \frac{\mathrm{d}\alpha}{f(\alpha)} = \int_0^{T} \frac{\upsilon}{\beta} \mathrm{e}^{-(E/RT)}\,\mathrm{d}T. \tag{10}$$

Eqs. (9) and (10) are applicable to rate-limiting mechanisms other than reaction front moving into a spherical grain, provided that proper kinetic expressions of $f(\alpha)$ and $g(\alpha)$ are used [5–10]. In these equations, v is the pre-exponential factor which includes many constants describing the initial state of the sample such as three-dimensional shape factors of initial particles, molecular mass, density, stoichiometric factors of chemical reaction, active surface and number of lattice imperfections, etc., as well as factors arising from the surface adsorption of gas and pressure. E is the activation energy for the rate-controlling process, R is the gas molar constant, and $k = v\mathrm{e}^{-(E/RT)}$ is the rate constant for the reaction. In Eq. (9), $f(\alpha)$ is expressible as an analytical function which is critically dependent on the rate-limiting reaction mechanism like random nucleation, diffusion, or phase boundary motion. The possible kinetic expressions for $f(\alpha)$ and $g(\alpha)$ are expressed in Table 1.

Note that [11]

$$\int_0^{T} \frac{\upsilon}{\beta} \mathrm{e}^{-(E/RT)}\,\mathrm{d}T \approx \frac{\upsilon}{\beta}\frac{RT^2}{E}\mathrm{e}^{-(E/RT)}, \tag{11}$$

so

$$\frac{g(\alpha)}{T^2} \approx \frac{\upsilon}{\beta}\frac{R}{E}\mathrm{e}^{-(E/RT)}$$

or

$$\ln\left(\frac{g(\alpha)}{T^2}\right) = -\frac{E}{RT} + \ln\left(\frac{\upsilon R}{\beta E}\right). \tag{12}$$

The implication of Eq. (12) is that the plot of $\ln\{[g(\alpha)]/T^2\}$ vs. $1/T$ is linear if the correct form of $g(\alpha)$ is chosen. The activation energy, E, and the pre-exponential factor, v, can be obtained from the slope and the intercept of such plot. A current practical approach among workers in the fields of TPD is to plot $\ln\{[g(\alpha)]/T^2\}$ vs. $1/T$ for all possible expressions of $g(\alpha)$ listed in Table 1. The rate-controlling mechanism corresponding to the $g(\alpha)$ expression that yields the most linear plot of $\ln\{[g(\alpha)]/T^2\}$ vs. $1/T$ is, then, considered to be consistent with the observed reaction.

Unfortunately, sometimes a few expressions of $g(\alpha)$ with very different values of E and v can yield plots of $\ln\{[g(\alpha)]/T^2\}$ vs. $1/T$ that are fairly linear [9]. Ambiguities concerning kinetic parameters and reaction mechanism can arise from such cases. In the following, we will strive to set an additional constraint which helps to eliminate $g(\alpha)$ expressions that yield incorrect kinetic parameters but, by coincidence, produce fairly linear plots of $\ln\{[g(\alpha)]/T^2\}$ vs. $1/T$. Note that at the onset of an activated decomposition (early few% of the decomposition curve vs. T), α may be approximated to be some constant and so is $f(\alpha)$. Then the activation energy of the decomposition process can be obtained from the slope of $\ln(\mathrm{d}\alpha/\mathrm{d}T)$ vs. I/T independent of the form of $f(\alpha)$

Table 1
Kinetic expressions of $f(\alpha)$ and $g(\alpha)$ for solid-state reactions

Symbol rate determining mechanism		$f(\alpha)$	$g(\alpha)$
Nucleation and growth models			
F1	(1) Mampel unimolecular law	$1-\alpha$	$-\ln(1-\alpha)$
A2	(2) Avrami–Erofeev nuclei growth – 2D	$2(1-\alpha)[-\ln(1-\alpha)]^{1/2}$	$[-\ln(1-\alpha)]^{1/2}$
A3	(3) Avrami–Erofeev nuclei growth – 3D	$3(1-\alpha)[-\ln(1-\alpha)]^{2/3}$	$[-\ln(1-\alpha)]^{1/3}$
A1	(4) Prout–Tompkins branching nuclei	$\alpha(1-\alpha)$	$\ln[\alpha/(1-\alpha)]$
Diffusion			
D1	Parabolic law – 1D	α^{-1}	$\alpha^2/2$
D2	2D diffusion	$[-\ln(1-\alpha)]^{-1}$	$(1-\alpha)\ln(1-\alpha)+\alpha$
D3	3D spherical diffusion (Jander)	$(1-\alpha)^{2/3}[(1-\alpha)^{-1/3}-1]^{-1}$	$1.5[1-(1-\alpha)^{1/3}]^2$
D4	3D diffusion (Brounshtein–Ginstling)	$[(1-\alpha)^{-1/3}-1]^{-1}$	$1.5[1-2\alpha/3-(1-\alpha)^{2/3}]$
Phase boundary movement			
R1	1D (zero order)	Constant	α
R2	2D (cylindrical symmetry)	$(1-\alpha)^{1/2}$	$2[1-(1-\alpha)^{1/2}]$
R3	3D (spherical symmetry)	$(1-\alpha)^{2/3}$	$3[1-(1-\alpha)^{1/3}]$
Power law		$(1-\alpha)^n$	$[1-(1-\alpha)^{1-n}]/(1-n)$

$$\ln\left(\frac{\mathrm{d}\alpha}{\mathrm{d}T}\right) = -\frac{E}{RT} + \ln\left(\frac{\upsilon}{\beta} f(\alpha)\right). \tag{13}$$

So if one plots $\ln(\mathrm{d}\alpha/\mathrm{dT})$ vs. I/T at the early onset of the decomposition curve, the slope of the plot yields correct value for E (even though nothing can be said about v or the reaction mechanism).

The criteria for choosing the right reaction mechanism and to obtain correct kinetic parameters in this work are then:

1. The reaction mechanism and kinetic parameters corresponding to the $g(\alpha)$ expression that yields the most linear plots of $\ln\{[g(\alpha)]/T^2\}$ vs. $1/T$ will be chosen.
2. If there are more than one $g(\alpha)$ satisfying the above condition, only the one that yields activation energy closest to E obtained from the plot of $\ln(\mathrm{d}\alpha/\mathrm{d}T)$ vs. I/T is chosen.

For convoluted TPD spectra, $f(\alpha) = f_1(\alpha) + f_2(\alpha) + \cdots$ and the application of the best linear fit to the plot of $\ln\{[g(\alpha)]/T^2\}$ vs. $1/T$ is not straightforward nor used in this work. Fortunately, deconvolution of convoluted TPD spectra by curve-fitting is possible. With the help of Eq. (11) and Table 1, Eq. (9) can be integrated to find an expression for $f(\alpha)$ in terms of E, v, β and T. This expression for $f(\alpha)$ can, then, be inserted back into Eq. (9) in the same fashion as done by Van Heek [11] such that computer curve-fitting is possible [1]:

$$\frac{\mathrm{d}\alpha}{\mathrm{d}T} = \left[\frac{\upsilon}{\beta}\mathrm{e}^{-(E/RT)}\right]\exp\left(-\frac{\upsilon}{\beta}\frac{RT^2}{E}\mathrm{e}^{-(E/RT)}\right) \quad \text{for F1,} \tag{14}$$

$$\frac{\mathrm{d}\alpha}{\mathrm{d}T} = \frac{\upsilon}{\beta}\mathrm{e}^{-(E/RT)}\left[1 - \frac{\upsilon}{3\beta}\frac{RT^2}{E}\mathrm{e}^{-(E/RT)}\right]^2 \quad \text{for R3,} \tag{15}$$

$$\frac{\mathrm{d}\alpha}{\mathrm{d}T} = \frac{\upsilon}{\beta}\mathrm{e}^{-(E/RT)}\left[1 - \frac{\upsilon}{2\beta}\frac{RT^2}{E}\mathrm{e}^{-(E/RT)}\right] \quad \text{for R2,} \tag{16}$$

$$\frac{\mathrm{d}\alpha}{\mathrm{d}T} = \frac{\upsilon}{\beta}\mathrm{e}^{-(E/RT)} \quad \text{for R1,} \tag{17}$$

$$\frac{\mathrm{d}\alpha}{\mathrm{d}T} = \frac{\upsilon}{\beta}\mathrm{e}^{-(E/RT)}\left[\frac{2\upsilon}{\beta}\frac{RT^2}{E}\mathrm{e}^{-(E/RT)}\right]^{-1/2} \quad \text{for D1,} \tag{18}$$

$$\frac{\mathrm{d}\alpha}{\mathrm{d}T} = \frac{\upsilon}{\beta}\mathrm{e}^{-(E/RT)}\left[1 - \left(\frac{\upsilon}{1.5\beta}\frac{RT^2}{E}\mathrm{e}^{-(E/RT)}\right)^{1/2}\right]^2 \times \left\{\left[1 - \left(\frac{\upsilon}{1.5\beta}\frac{RT^2}{E}\mathrm{e}^{-(E/RT)}\right)^{1/2}\right]^{-1} - 1\right\}^{-1} \quad \text{for D3,} \tag{19}$$

$$\frac{\mathrm{d}\alpha}{\mathrm{d}T} = \frac{\upsilon^2}{\beta^2}\frac{RT^2}{E}\mathrm{e}^{-2(E/RT)}\left[2\exp\left\{-\left(\frac{\upsilon}{\beta}\frac{RT^2}{E}\mathrm{e}^{-(E/RT)}\right)^2\right\}\right] \quad \text{for A2,} \tag{20}$$

$$\frac{\mathrm{d}\alpha}{\mathrm{d}T} = \frac{\upsilon^3}{\beta^3}\frac{R^2T^4}{E^2}\mathrm{e}^{-3(E/RT)}\left[3\exp\left\{-\left(\frac{\upsilon}{\beta}\frac{RT^2}{E}\mathrm{e}^{-(E/RT)}\right)^3\right\}\right] \quad \text{for A3,} \tag{21}$$

$$\frac{\mathrm{d}\alpha}{\mathrm{d}T} = \frac{\upsilon}{\beta}\mathrm{e}^{-(E/RT)}\left[\frac{\exp\left(\frac{\upsilon}{\beta}\frac{RT^2}{E}\mathrm{e}^{-(E/RT)}\right)}{1+\exp\left(\frac{\upsilon}{\beta}\frac{RT^2}{E}\mathrm{e}^{-(E/RT)}\right)}\right] \times \left[1 - \frac{\exp\left(\frac{\upsilon}{\beta}\frac{RT^2}{E}\mathrm{e}^{-(E/RT)}\right)}{1+\exp\left(\frac{\upsilon}{\beta}\frac{RT^2}{E}\mathrm{e}^{-(E/RT)}\right)}\right] \quad \text{for A1.} \tag{22}$$

In Fig. 1, using expressions (14)–(16), we show simulated TPD spectra of $\mathrm{d}(\alpha)/\mathrm{d}T$ with $E \approx 84$ kJ/mol, $v = 10^7$ s^{-1}, and a ramp rate of 1 K/s for processes controlled by unimolecular random nucleation (F1), 2D-phase boundary motion (R2), and 3D-phase boundary motion (R3). Note that the shape of $\mathrm{d}(\alpha)/\mathrm{d}T$ for unimolecular random nucleation process tends to be much more symmetrical than that for 3D-phase boundary motion. As one proceeds to 2D-phase boundary motion, the shape of $\mathrm{d}(\alpha)/\mathrm{d}T$ becomes even more asymmetrical. The illustration in Fig. 1 points to the fact that the shapes of TPD spectra corresponding to the many rate-controlling mechanisms are distinctive (cf. Footnote 1). Some prior knowledge of the reaction mechanism(s) near the onset or the end of the TPD process would be helpful when curve fitting convoluted TPD spectra with the various expressions for $\mathrm{d}(\alpha)/\mathrm{d}T$ listed above. In this curve-fitting technique, the combination of particular expressions of $\mathrm{d}(\alpha)/\mathrm{d}T$ that yield the best curve fit is said to be consistent with the observed TPD spectra.

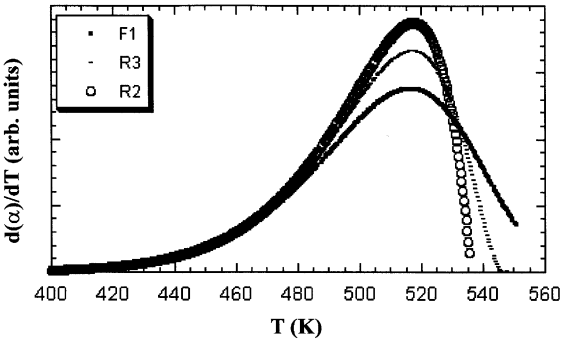

Fig. 1. The shapes of many reaction rates with different reaction mechanisms can be distinctively seen in this simulation with $E = 20$ kJ/mol and $v = 10^7$ s^{-1} and a ramping rate of 1 K/s. F1, R3, and R2 are reaction mechanisms defined in Table 1.

[1] Due to the various approximations made [e.g. in obtaining Table 1 and Eq. (10)], when doing computer fitting, one should be aware that many of the following expressions may not be well-behaved far beyond the decomposition peaks.

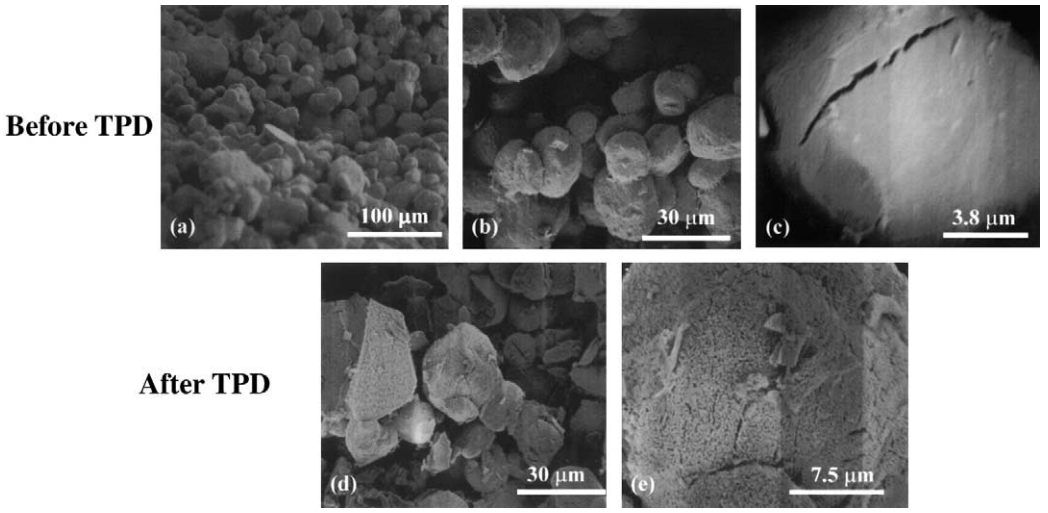

Fig. 2. SEM images of LiOH powders before TPD (a)–(c) and after TPD (d) and (e).

4. Experimental results and discussion

4.1. TPD of LiOH powders

Figs. 2(a)–(c) show scanning electron microscopy (SEM) images of LiOH powders before TPD. The powders had grain size in the range of 10–50 μm and there were cracks on some grains. Figs. 2(d) and (e) show SEM images of LiOH powders after TPD. Substantially more cracks, a lot of debris (Fig. 2(d)) and a porous structure (Fig. 2(e)) common in many grains were observed in these powders after TPD. This is probably a result of lattice structure change from cubic with lattice parameter of $a = 4.611$ Å for Li_2O to tetragonal with lattice parameters of $a = 3.553$ Å and $c = 4.348$ Å for LiOH.

In Fig. 3(a), we show the fractional decomposition rate of LiOH powders under a linear heating ramp rate of 0.46 K/s. In comparison with Fig. 1, unimolecular random nucleation (F1) cannot be a possible reaction mechanism in this sample, since the shape of $d(\alpha)/dT$ for LiOH powders in Fig. 3(a) is very asymmetrical and similar to those for phase boundary motion. Fig. 3(b) shows a plot $\ln(d\alpha/dT)$ vs. $1/T$ near the onset of the decomposition process according to Eq. (13). The best linear fit to the plot yields an activation energy of about 135 kJ/mol. The error associated with this technique is ~10%. The plot of $\ln[g(\alpha)\,T^{-2}]$ vs. $1/T$ according to Eq. (12) with $g(\alpha)$ representing the kinetic expression for 3D-phase boundary movement ($R3$) yields the best straight line with $E \sim 136$ kJ/mol and $v \sim 6.9 \times 10^9$ s^{-1} and is presented in Fig. 3(c). With an activation energy for the decomposition of ~136 kJ/mol and a pre-exponential factor on the order of 6.9×10^9 s^{-1}, LiOH is very stable at room temperature. The decomposition of LiOH powders at a constant temperature as a function of time with 3D-phase boundary motion as the rate-controlling process can be written from Eq. (8) and Table 1 as follows:

$$\alpha(t) = 1 - \left\{1 - \left[\frac{v}{3} t\, e^{-(E/RT)}\right]\right\}^3. \tag{23}$$

Fig. 4 shows the decomposition simulation curves for LiOH powders using the kinetic parameters obtained above. The decomposition of LiOH into Li_2O by releasing H_2O is minimal even at 320 K over 100 years as would be typically expected for solid reactions with an activation energy in the range of $\geqslant$120 kJ/mol.

4.2. TPD of an LiD single crystal previously exposed to ambient air at approximately 30–40% relative humidity

In Fig. 5(a)–(c), we show cross-section SEM images of a typical LiOH film grown in air with 30–40% relative humidity. Columnar growth is clearly observed for the LiOH film grown on the LiD single substrate. Fig. 5(d) shows the SEM image of the same film looking from the top down. Columnar structures with voids and opened space are distinctly seen in this image. For films with thickness on the order of micrometers, the growth rate of LiOH and/or LiOH · H_2O on LiD around this level of relative humidity is found to be on the order of 0.1 nm/s and is linear with time, suggesting that the process is not controlled by H_2O diffusion in the films. A possible pathway for H_2O to reach the LiD single crystal substrate to grow LiOH and/or LiOH · H_2O linearly with time is through cracks or opened space in the films as observed in Fig. 5(d).

Fig. 6(a) shows the TPD curve of an LiD single crystal previously exposed to ambient air for 8 min. This

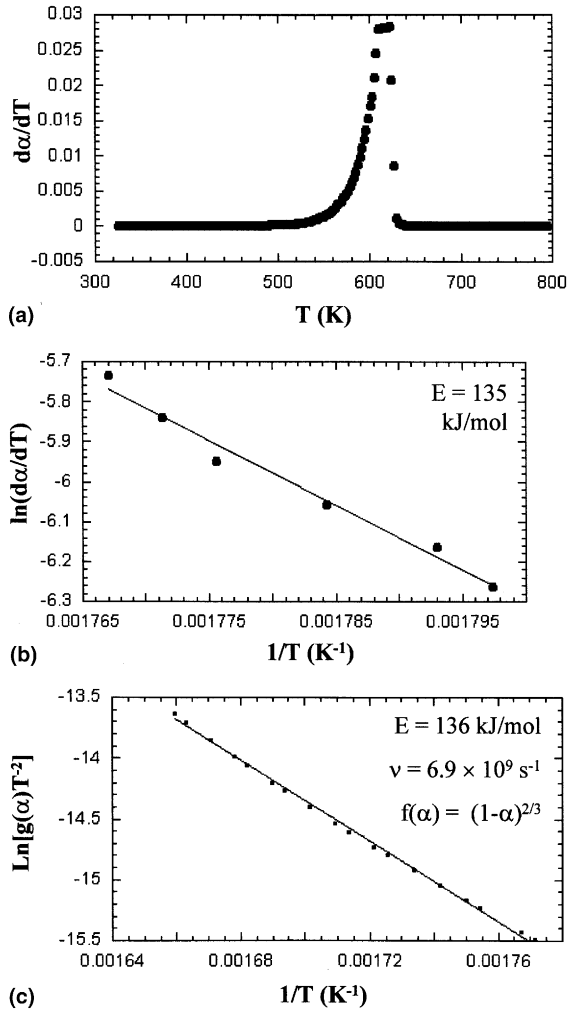

Fig. 3. Fractional decomposition rate of LiOH powders under a linear heating schedule of 0.46 K/s (a); plot $\ln(\mathrm{d}\alpha/\mathrm{d}T)$ vs. $1/T$ near the onset of the decomposition process (b); plot of $\ln[g(\alpha)\,T^{-2}]$ vs. $1/T$ with $g(\alpha)$ representing the kinetic expression for 3D-phase boundary movement (R3).

sample was pumped for a few hours following the moisture exposure step and before the TPD experiment. The portion of the TPD spectrum between 450 and 570 K is not convoluted and a plot of $\ln\{[g(\alpha)]/T^2\}$ vs. $1/T$ for different $g(\alpha)$ expressions in Fig. 6(b) reveals that unimolecular random nucleation (F1) is a consistent rate-controlling mechanism in this temperature window with an activation energy of 97–100 kJ/mol and a pre-exponential factor of 7.18×10^7–1.4×10^8 s^{-1}. The portion of the TPD spectrum between 300 and 450 K is slightly convoluted. The deconvolution presented in Fig. 6(c) yields two separate decomposition processes with unimolecular random nucleation (F1) as rate-controlling

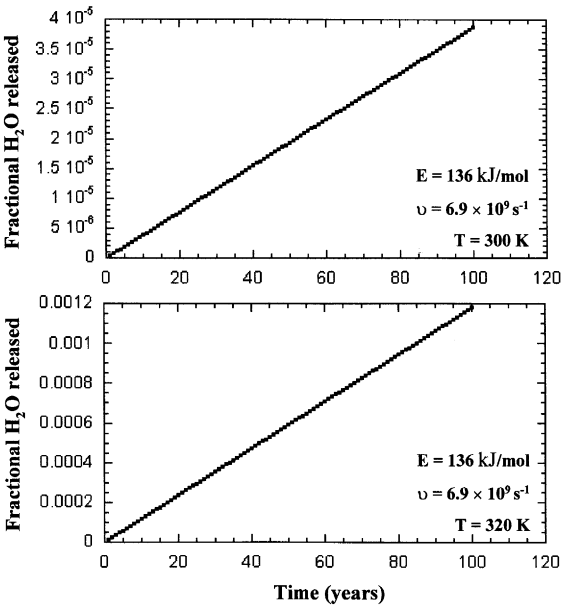

Fig. 4. Decomposition simulation curves for LiOH powders.

mechanism. Curve-fit (I) has $E = 48$–59 kJ/mol and $v = 2.4 \times 10^5$–7.5×10^6 s^{-1}. Curve-fit (II) has $E = 63$–67 kJ/mol and $v = 2.0 \times 10^6$–9.5×10^6 s^{-1}. The portion of the TPD spectrum around 640 K appears to contain up to four convoluted decomposition curves with unknown rate-controlling kinetics. Unambiguous deconvolution of the spectrum here is not simple. However, from the analysis of the previous sample, the peak position in this region corresponds to an activation energy in the range of 122–149 kJ/mol. This peak is stable and provides no practical interest.

The H_2O peaks corresponding to curve fits (I) and (II) are attributed to water molecules in the LiOH · H_2O structure formed during 8 min of moisture exposure prior to TPD experiment. Figs. 7(a) and (b) show the simulated release of H_2O from LiOH · H_2O structures with $E = 48$ and 67 kJ/mol. The simulation curve for a dehydration or a decomposition process with unimolecular random nucleation (F1) as the rate-controlling mechanism can be written in the same fashion as Eq. (23)

$$\alpha(t) = 1 - \exp\left[-t\upsilon \mathrm{e}^{-(E/RT)}\right]. \tag{24}$$

It can be seen from the figure that H_2O molecules from LiOH · H_2O structures can be effectively pumped away at room temperature. Two days of pumping at room temperature is enough to remove essentially all H_2O from the LiOH · H_2O structures. Fig.7(c) shows the simulated decomposition of LiOH structure with $E = 97$ kJ/mol and with unimolecular random nucle-

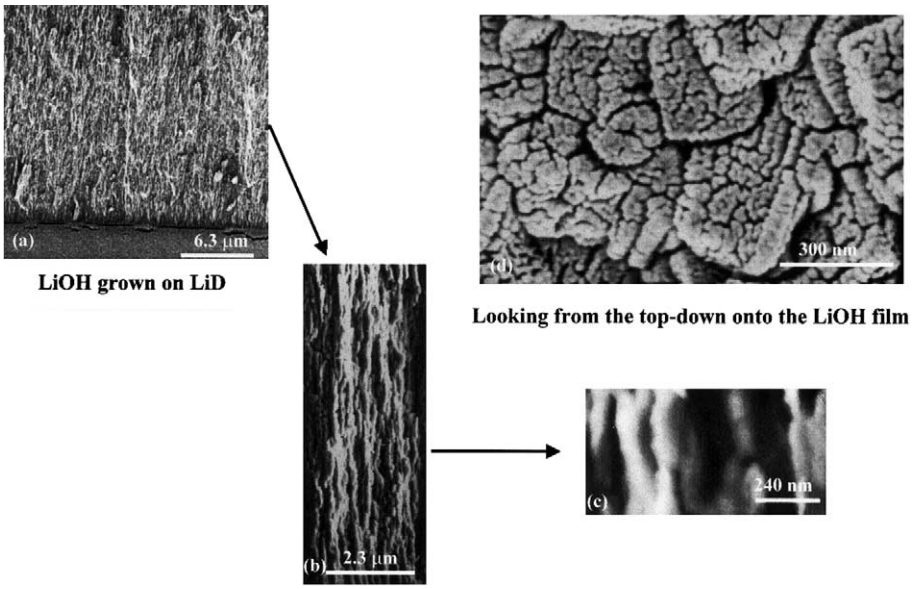

Fig. 5. Cross-section SEM images of a typical LiOH film grown in air with 30–40% relative humidity (a)–(c) and SEM image of the same film looking from the top down (d).

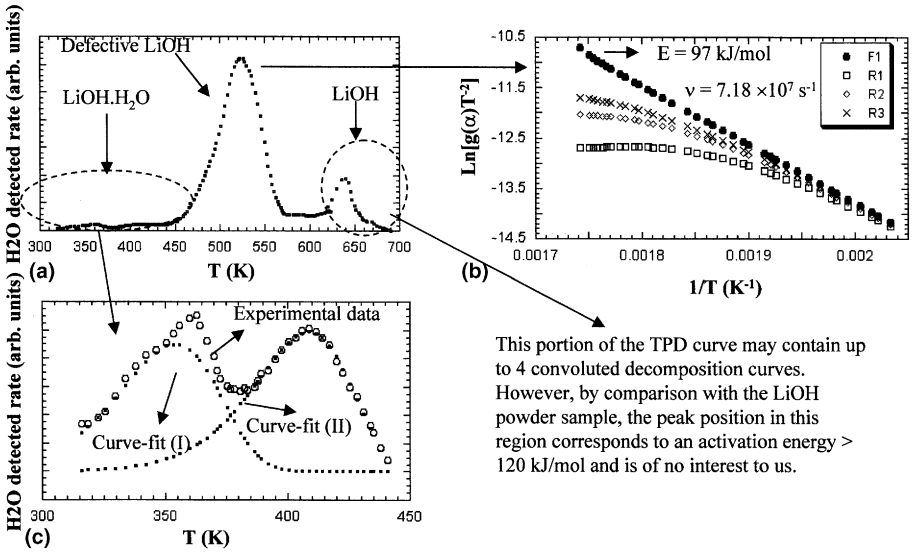

Fig. 6. TPD spectrum of an LiD single crystal previously exposed to ambient air for 8 min (a); plot of $\ln\{[g(\alpha)]/T^2\}$ vs. $1/T$ for different $g(\alpha)$ expressions (b); and the deconvolution of the portion of the TPD spectrum in the window of 300–450 K (c).

ation (F1) as the rate-controlling mechanism at room temperature. This LiOH structure with a low activation energy of decomposition of $E = 97$ kJ/mol will severely decompose in the next 100 years. At this point, we attribute the H_2O peaks around 530 K ($E = 97$–100 kJ/mol) to the decomposition of sub-stoichiometric LiOH or $Li(OH)_x$ with $x < 1$ and defective LiOH structures with a lot of cracks, broken bonds and other disorders. The H_2O peak around (640 K) is attributed to the decomposition of high quality LiOH. $Li(OH)_x$ should be formed more favorably under low moisture exposure conditions. This is similar to the case of SiO_2 and SiO_x with $x < 1$. In many cases, SiO_x was found to be a network of SiO_2 with a lot of defects such as oxygen vacancies and broken or dangling bonds [12]. Thermodynamically, SiO_x is not stable and will convert

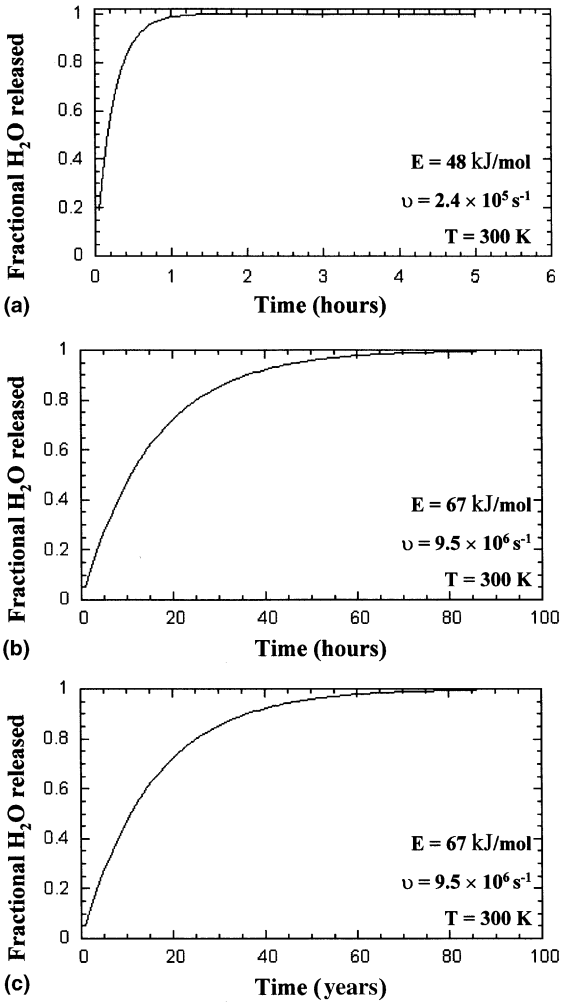

Fig. 7. The simulated release of H_2O from $LiOH \cdot H_2O$ structures (a) and (b) and the decomposition of the LiOH structure with $E = 97$ kJ/mol at room temperature (c).

to SiO_2, but kinetically this may take a long time at room temperature. This is the reason why oxide grown on the surface of a Si wafer still has $x < 2$ after many years of air exposure. This oxide can be removed by simply flash-heating the Si wafer in a vacuum to around 1000°C while true SiO_2 films are stable even at much higher temperatures [13]. An alternate explanation for the multi-activation energy barriers observed for the decomposition of LiOH is that the process originated from a sub-monolayer effect or layer-by-layer decomposition. If this is the case, the effect should be even more pronounced for thicker LiOH films and is independent of the moisture levels in which the different LiOH films grow as long as the films have the same thickness. We will see if this is true in the following sections.

4.3. TPR of an LiD single crystal previously exposed to air for 2 h at approximately 30–40% relative humidity

Fig. 8(a) shows the TPD spectrum of an LiD single crystal previously exposed to ambient air for 2 h. Unfortunately, due to experimental difficulty with the heating system below 450 K, only data in the 450–700 K are presented here. The TPD data reveal that the decomposition of LiOH into Li_2O and H_2O has multiple activation energy barriers between 450 and 700 K. The deconvolution yields two separate decomposition processes and is presented in Fig. 8(b). Curve-fit (I) corresponds to a decomposition process with unimolecular random nucleation (F1) as the rate-controlling mechanism. Its kinetic parameters are: $E = 109$–124 kJ/mol, $v = 1.53 \times 10^8$–5.95×10^9 s^{-1}. Curve-fit (II) corresponds to a decomposition process with either a 2D or 3D-phase boundary motion (R2 or R3) as the rate-controlling mechanism. Its kinetic parameters are: $E = 122$–135 kJ/mol and $v = 4.60 \times 10^8$–6.41×10^9 s^{-1}. Due to the columnar structures of LiOH films grown on LiD single crystal substrates, the conversion of LiOH to Li_2O corresponding to curve-fit (II) can be most accurately described by a phase boundary motion in a cylindrical symmetry. If we call Z and R the average height

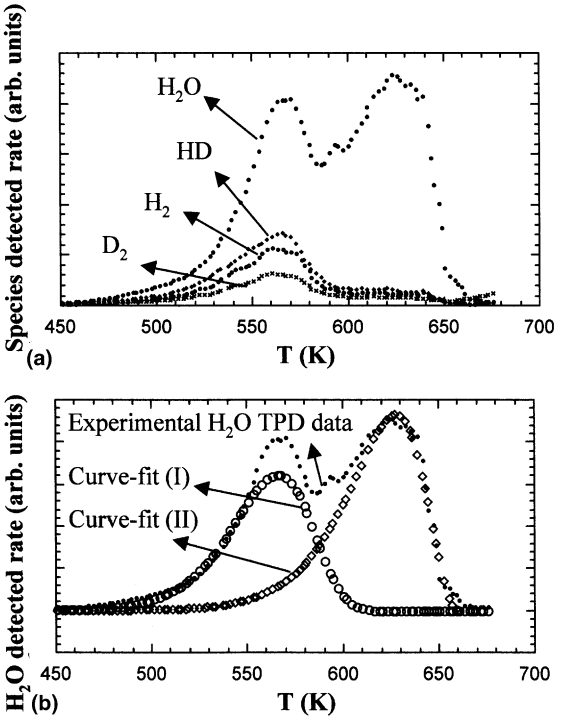

Fig. 8. TPD spectrum of an LiD single crystal previously exposed to ambient air for 2 h (a) and the deconvolution of the spectrum into two separate decomposition processes (b).

and radius of these columnar structures, then with the assumption

$$\frac{dr}{dt} = \frac{dz}{dt} = -\kappa, \tag{25}$$

one can write

$$r = R - \kappa t \quad \text{and} \quad z = Z - \kappa t. \tag{26}$$

Moreover, the reacted fraction is

$$\alpha = 1 - \frac{r^2 z}{R^2 Z} = 1 - \left[\left(1 - \frac{\kappa}{R}t\right)^2 \left(1 - \frac{\kappa}{Z}t\right)\right]. \tag{27}$$

For very thin LiOH films ($Z \ll R$), the LiOH to Li_2O conversion of LiOH film on LiD is a one-dimensional phase boundary motion with $\alpha \approx 1 - (z/Z)$. This is the model proposed by Meyers: a reaction front moving inward from the surface with the release of H_2O into the vacuum, and a reaction front moving upward from the interface releases H_2O to react with the underlying substrate [1]. However, for very thick films ($Z \gg R$), one deals essentially with a 2D phase boundary motion along the radial direction with $\alpha \approx 1 - (r^2/R^2)$.

For Z and R with comparable dimensions, Eq. (27) describes a 3D-phase boundary motion in a cylindrical grain. In all cases, some of the H_2O released advances toward the vacuum while some proceeds toward the LiD substrate to react.

For a linear heating schedule with a ramp rate of β

$$\alpha = 1 - \left\{\left[1 - \frac{\kappa}{R}\left(\frac{T - T_0}{\beta}\right)\right]^2 \left[1 - \frac{\kappa}{Z}\left(\frac{T - T_0}{\beta}\right)\right]\right\}. \tag{28}$$

Eq. (28) can be solved numerically for κ as a function of T for each value of α if Z and R are known. Fig. 9(a) shows the plot of α vs. T for the portion of the TPD data obtained by subtracting the raw TPD data by curve-fit (I). Taken $2R = 90$ nm (grain width obtained from SEM images ranged from 30 to 150 nm), $Z = 720$ nm (from a linear growth of LiOH of ~0.1 nm/s), and $\beta = 0.46$ K/s, a plot of κ vs. T was obtained by solving Eq. (28) numerically for each α value in the range of 0.2–0.8 and is presented in Fig. 9(b). When the plot in Fig. 9(b) is fitted with $\kappa = \kappa_o e^{-(E/RT)}$, one obtains $E \sim 122$–129 kJ/mol and $\kappa_0 \sim 5.4 \times 10^8$–$2.4 \times 10^9$ nm s^{-1}.

The decomposition curve (I) has a smaller activation energy barrier and is again attributed to the decomposition of defective and/or sub-stoichiometric LiOH. The decomposition curve (II) has a higher activation energy barrier and is attributed to the decomposition of good quality LiOH. We observe that the rate-controlling mechanism for good quality LiOH is the same as that of LiOH powders presented earlier, namely inward moving reaction front(s). We also notice that the amounts of HD, H_2, and D_2 detected in Fig. 8(a) were only a fraction of the amount of H_2O detected. In a vacuum or dry environment, due to a lack of supply of H_2O molecules to the LiOH/LiD interface, LiD reacts with LiOH to form Li_2O and hydrogen species instantaneously at the interface according to the reaction

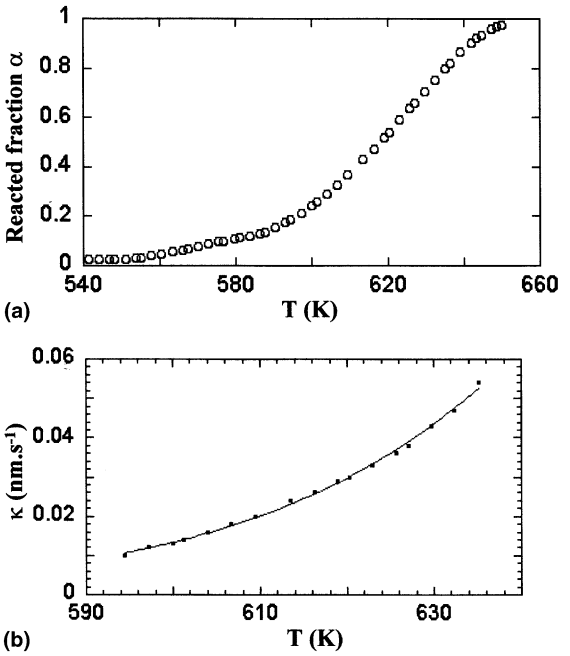

Fig. 9. The plot of α vs. T (a) for the portion of the TPD data obtained by subtracting the raw TPD data of Fig. 8 by curve-fit (I). With $2R = 90$ nm, $Z = 720$ nm, and $\beta = 0.46$ K/s, a plot of κ vs. T was obtained by solving Eq. (28) numerically for each α value in the range of 0.2–0.8 (b). When this plot is fitted with $\kappa = \kappa_0 e^{-(E/RT)}$, one obtains $E \sim 122$–129 kJ/mol and $\kappa_0 \sim 5.4 \times 10^8$–$2.4 \times 10^9$ nm s^{-1}. The solid line represents the curve-fit.

$$\mathrm{LiD} + \mathrm{LiOH} \rightarrow \mathrm{Li_2O} + \mathrm{aH_2\ (g)} + \mathrm{bHD\ (g)} + \mathrm{cD_2\ (g)}, \tag{29}$$

where $\mathrm{aH_2\ (g)} + \mathrm{bHD\ (g)} + \mathrm{cD_2\ (g)} = \mathrm{1H} + \mathrm{1D}$.

Reaction (29) has a negative ΔG (Gibbs free energy) even at 273 K and the formation of an LiD/Li_2O/LiOH interface at room temperature in a dry environment is guaranteed.

Experimental evidence for the existence of a LiH/Li_2O/LiOH interface has been reported by McLaughlin and Cristy [14]. However, the hydrogen species observed in the TPD spectrum of Fig. 8(a) were detected at a rather elevated temperature, certainly after the formation of a LiH/Li_2O/LiOH interface much earlier on during the many hours of pumping time in the vacuum chamber. During the decomposition of LiOH according to Eq. (1), some of the H_2O released goes

toward the LiD/Li_2O interface to react with LiD according to

$$2LiD + H_2O \rightarrow Li_2O + dH_2\ (g) + eHD\ (g) + fD_2\ (g), \quad (30)$$

where $dH_2\ (g) + eHD\ (g) + fD_2\ (g) = 2H + 2D$.

So, both reactions (1) and (30) happened during the decomposition of LiOH structures grown on LiD single crystals reported here. However, the hydrogen species evolved most heavily near the region of decomposition dominated by LiOH structures with more defects (Fig. 8(a)). This suggests that there are more defects in the LiOH structure near the single crystal $LiD/Li_2O/LiOH$ interface. This is expected due to a change in lattice structures and volume in going from single crystal LiD to Li_2O and to LiOH.

The LiOH film grown by air exposure at 30–40% relative humidity for 2 h was roughly 720 nm thick and almost 15 times thicker than the one grown in 8 min. It is expected that in the absence of $Li(OH)_x$ and other defective LiOH, the multiple activation energy effects exhibited in TPD should be more pronounced for thicker films if sub-monolayer effects or layer-by-layer decomposition of LiOH really happens. This is not what is observed in Figs. 6 and 8. In fact, the opposite is observed here: the LiOH decomposition peaks for the much thicker LiOH film (Fig. 8) were much closer together (smaller difference in activation energies) than the ones for the thinner LiOH film (Fig. 6). On the other hand, if the multiple LiOH decomposition peaks in Figs. 6 and 8 are due to defective LiOH structures near the $LiD/Li_2O/LiOH$ interface and good quality LiOH structures, the effect should be less pronounced when the LiOH film is thicker. This is because as the film gets thicker, the fraction of substoichiometric and defective LiOH, which is located near the $LiD/Li_2O/LiOH$ interface region becomes smaller. This is what we observe in Figs. 6 and 8. In Fig. 6, the LiOH film is thin and the ratio of defective LiOH to good quality LiOH is high. In Fig. 8, the LiOH film is thick and the ratio of defective LiOH to good quality LiOH is small. So the possibility of sub-monolayer effects or layer-by-layer decomposition of LiOH is ruled out in this work in favor of the existence of sub-stoichiometric $Li(OH)_x$ and defective LiOH near the single crystal LiD/Li2O/LiOH interface.

4.4. TPD of LiD which had been annealed to 503 K for 48 h, cooled down to room temperature, then exposed to different dosages of H_2O

In this set of experiments, an LiD single crystal, which had been annealed to 503 K for 48 h in an ultrahigh vacuum environment and then cooled down to room temperature, was exposed to 39 ppm of moisture for 4 h prior to TPD experiment. After that, the same sample was subjected to the same heating and cooling cycle described above, then exposed to 399 ppm of moisture for 3.2 h prior to TPD experiment. A similar heating and cooling cycle was applied to the sample before it was exposed once again to moisture at 779 ppm for 20 h. The upper part of Fig. 10 shows the TPD spectra of this sample after three separate moisture exposures. It is noted that as the level of water exposure increased, the first TPD peak shifted to higher temperature, implying an increase in the activation energy of decomposition of defective LiOH. These TPD spectra are very heavily convoluted and are not easy to be deconvolved. However, without deconvoluting the spectra, the Arrhenius plot based on Eq. (13) can be used to

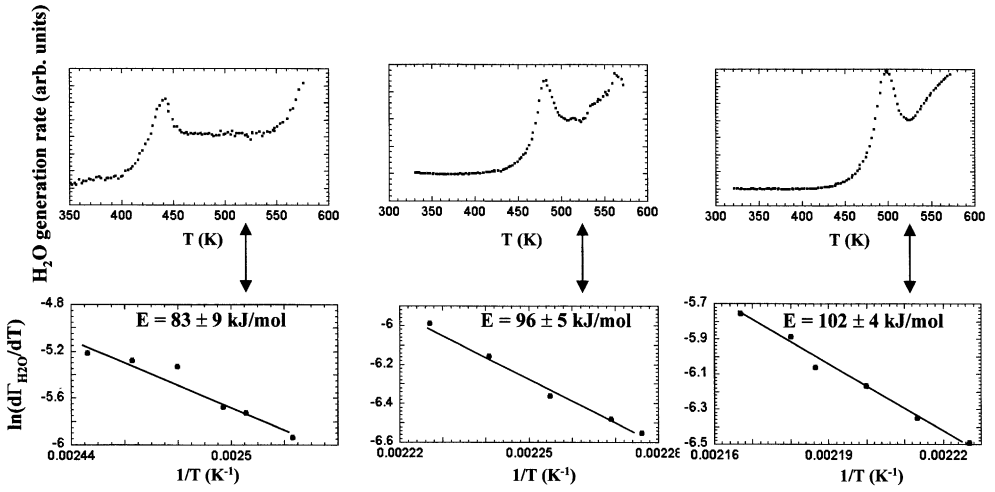

Fig. 10. TPD spectra of the same sample after three separate moisture exposures (upper part) and the Arrhenius plots for the determination of the activation energies of decomposition in the three cases.

obtain the lower end of the activation energies of decomposition for defective/sub-stoichiometric LiOH. In the lower part of Fig. 10, we show the Arrhenius plot for the determination of the activation energies of decomposition in the three cases. In these plots, Γ_{H2O} designates the flux of H_2O detected by the mass-spectrometer. Activation energies as low as 83 ± 9, 96 ± 5, and 102 ± 4 kJ/mol have been found for the decomposition of defective LiOH that formed under moisture exposure conditions of 39 ppm for 4 h, 399 ppm for 3.2 h, and 779 ppm for 20 h. It is seen, here, that the lower levels of moisture exposure formed 'poorer quality' LiOH which decomposed at lower temperatures than the 'better quality' LiOH formed at higher levels of moisture exposure. So, in general, we observe that at lower exposure dosages, the LiOH formation on single crystal LiD is highly defective and has components which tend to decompose at activation energy barrier as low as 83 kJ/mol. Even though the effect of repeated moisture exposure followed by TPD annealing on the activation energy of decomposition of defective LiOH is not studied in this report, we feel confident that lower moisture exposures tend to form more defective/sub-stoichiometric LiOH which decompose with lower activation energies. This is confirmed by the fact that two LiOH films reported in Figs. 6 and 8 follow this same trend even though they were not subjected to repeated moisture exposure/TPD cycles.

4.5. The reaction of LiD with moisture at elevated temperatures

Fig. 11 shows that the reaction of LiD with moisture is significantly reduced at elevated temperatures, even at atmospheric pressures with 50% relative humidity. From the figure, it is seen that at 50% relative humidity, air exposure of the LiD single crystal labeled 'Sample a' for 30 h at $T = 300$ K resulted in ~18 μm thick of reacted layer (LiOH and/or $LiOH \cdot H_2O$). 'Sample a' and 'Sample b' were originally from the same LiD single crystal which was subsequently cleaved into two smaller pieces. 'Sample b' was subjected to the same moisture exposure conditions as 'Sample a', except at a slightly elevated temperature of $T = 339$ K. The reacted layer from 'Sample b' was less than a few micrometers in thickness. We attribute the much more reduced reaction rate of LiD with moisture at elevated temperatures to the reduced sticking probability of H_2O molecules on a hot surface.

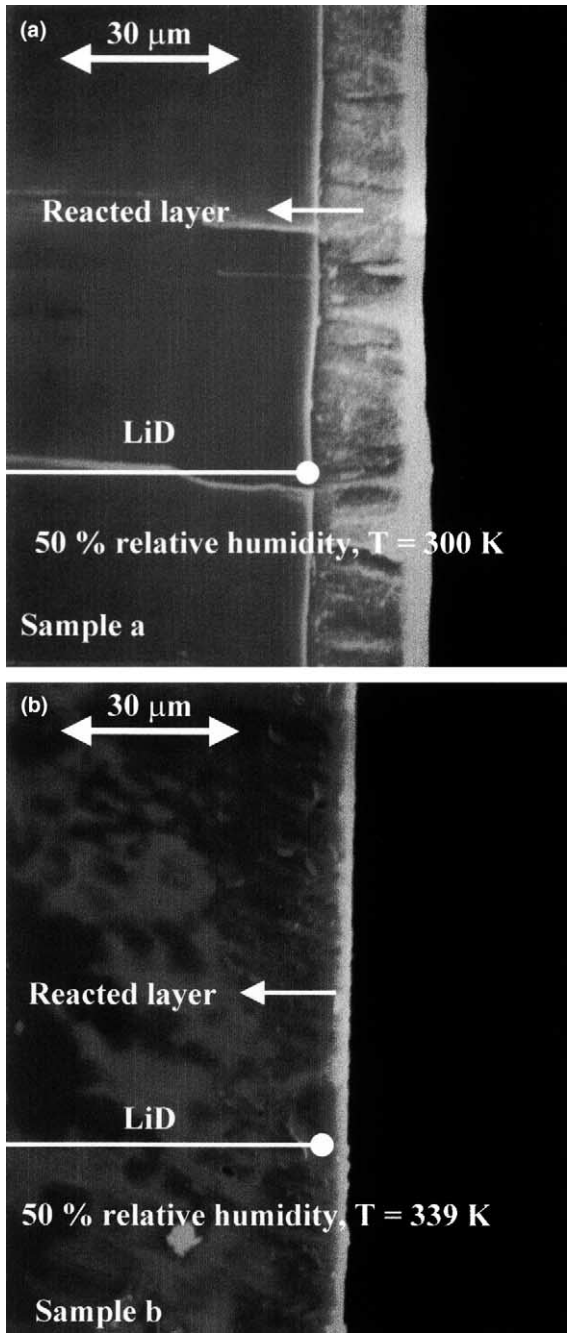

Fig. 11. SEM shows that the reaction of LiD with moisture is greatly reduced at elevated temperatures.

5. Conclusions

We have performed TPD on LiOH powders and LiD single crystals, which had been previously exposed to different moisture levels. Our results show that the decomposition process of LiOH has a high activation energy barrier of between 122 and 149 kJ/mol (in agreement with the result reported by Myers [1]) and the rate-controlling mechanism for this process is consistent with an inward phase boundary motion. This LiOH structure is stable even if kept at an elevated temperature

of 320 K. However, LiOH structures grown on single crystal LiD at low levels of moisture exposure may have an activation energy barrier much lower than 122 kJ/mol. This activation energy barrier decreases with decreasing moisture exposure level and has a rate-controlling mechanism consistent with a unimolecular random nucleation process. We attribute the low activation energy barriers for the decomposition of these LiOH structures formed at low levels of moisture exposure to the existence of broken bonds, cracks, and other long-range disorders in the LiOH structures and/or $Li(OH)_x$ with $x < 1$. These defective LiOH structures may decompose significantly over many years of storage even at room temperature. At very high moisture exposure levels, the release of H_2O molecules from $LiOH \cdot H_2O$ structure has a small activation energy barrier of between 48 and 67 kJ/mol and follows a unimolecular nucleation process. The loosely bonded H_2O molecules can be easily pumped away at room temperature in a reasonable amount of time. Finally, our experiments suggest that handling LiD at an elevated temperature of 340 K or more efficiently reduces the growth of LiOH and $LiOH \cdot H_2O$.

Acknowledgements

This work was performed under the auspices of the US Department of Energy by the University of California, Lawrence Livermore National Laboratory under contract no. W-7405-ENG-48.

References

[1] S.M. Myers, J. Appl. Phys. 45 (1974) 4320.
[2] H. Kudo, J. Nucl. Mater. 87 (1979) 185.
[3] L.N. Dinh, M. Balooch, J.D. LeMay, UCRL-ID-135387, Lawrence Livermore National Laboratory.
[4] J.M. McIntyre, H.M. Smith, American Chemical Society Paper Abstract for the S.E. and S.W. Regional Meeting, December 2–4, 1970, p. 174.
[5] D.A. Young, Decomposition of Solids, Pergamon, New York, 1966.
[6] W.E. Garner, Chemistry of the Solid State, Academic, New York, 1955 (Chapter 7).
[7] C.H. Bamford, T.C.H. Tipper, Comprehensive Chemical Kinetics: Reaction in the Solid State, vol. 22, Elsevier, Amsterdam, 1980, p. 41.
[8] K. Heide, W. Holand, H. Golker, K. Seyfarth, B. Muller, R. Sauer, Thermochim. Acta 13 (1975) 365.
[9] A.M. Gadalla, Thermochim. Acta 95 (1985) 179.
[10] S. Dash, M. Kamruddin, P.K. Ajikumar, A.K. Tyagi, B. Raj, S. Bera, S.V. Narasimhan, J. Nucl. Mater. 278 (2000) 173.
[11] K.H. Van Heek, H. Juntgen, Beri. Deutsch. Bunsengesells. Physikal. Chem. 72 (1968) 1223.
[12] L.N. Dinh, L.L. Chase, M. Balooch, F. Wooten, W.J. Siekhaus, Phys. Rev. B 54 (1996) 5029.
[13] L.N. Dinh, M. Balooch, unpublished.
[14] J.F. McLaughlin, S.S. Cristy, Composition of Corrosion Films on Lithium Hydride Surfaces After Exposure to Air, Oak Ridge Y-12 Plant, 1974.